Nanoscale

Accepted Manuscript

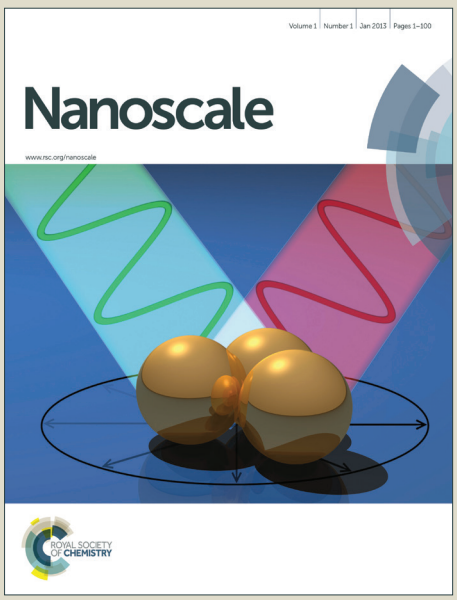

ROYAL SOCIETY OF CHEMISTRY

www.rsc.org/nanoscale

Nanoscale

PAPER

Compressible Elastomeric Aerogels of Hexagonal Boron Nitride and Single-wall Carbon Nanotubes

Received 00th January 20xx,
Accepted 00th January 20xx

DOI: 10.1039/x0xx00000x

www.rsc.org/

Yeon Joo Jeong and Mohammad F. Islam*

Lightweight porous ceramic materials that can recover their shapes after mechanical deformation have numerous applications. However, this type of materials tends to be highly fragile and often crack when compressed. Here, we report on fabrication and characterization of highly porous, freestanding composites of hexagonal boron nitride (h-BN) and single-wall carbon nanotubes (SWCNTs) of density 13–15 mg/mL, which corresponds to a volume fraction of 0.009, that were mechanically robust and recovered their original shape even after uniaxially compressing them by more than 50%. We made these porous elastomeric composites using solution based assembly process that involved first shaping SWCNTs into porous networks of density ~7 mg/mL (volume fraction ~0.005) followed by coatings of SWCNT networks with 6–8 mg/mL of h-BN (volume fraction ~0.003–0.004). The h-BN coating strengthened the underlying SWCNT networks, likely via reinforcement of the nodes between the SWCNTs, resulting in an increase in Young's modulus by ~100% compared to that of SWCNT networks alone. Surprisingly, SWCNT networks, which were initially highly fragile, became elastomeric after h-BN coating, even though porous structures solely from h-BN are very brittle. Our fabrication approach preserves the morphology of the underlying networks, allowing for fabrication of various shapes and sizes of porous composites of h-BN and SWCNTs. Finally, our fabrication scheme is robust and facile to prepare porous composites of diverse ceramic materials and SWCNTs using appropriate ceramic-precursor.

Introduction

Three-dimensional (3D), lightweight, highly porous structures, which are also referred to as aerogels and foams, are of great interest due to their broad technological applications.[1-13] Typically, the intrinsic properties of the materials that make up aerogels as well as the pore geometry and the volume fraction dictate the foam properties and their applications.[14] Consequently, several functional materials such as graphene, graphene oxide, carbon nanotubes, boron nitrides have been utilized to fabricate 3D foams that retain any or all of the properties of these nanoscale components.[9,12,15-20] Chemical vapour deposition (CVD) process is perhaps the widely used fabrication method to produce foams of nanomaterials, often using porous scaffolds as sacrificial templates, particularly for foams of graphene or hexagonal boron nitrides (h-BN).[18,21,22] However, CVD grown porous structures have limitations in shapes and sizes,[23,24] are frequently burdened with impurities,[25,26] and become prohibitively expensive to scale up.[17]

Recently, solution processed assembly of nanomaterials with or without porous sacrificial templates has attracted great interest because this approach allows use of well-characterized nanomaterials, provides foams with tunable shapes and sizes, and is inexpensive to scale up.[16,23,24] Furthermore, this approach may potentially allow fabrication of foams from two or more types of nanomaterials; such composite foams may possess emergent properties that are not displayed by foams of either of the pure components. For example, we assembled purified, individually dispersed single-wall carbon nanotubes (SWCNTs) in water into freestanding aerogels that possessed ultrahigh specific surface area (SSA) and high electrical conductivity arising from intrinsic properties of SWCNTs.[6,14] The SWCNTs within these aerogels were arranged in a porous, isotropic network with an open-cell structure that was held together primarily via van der Waals interactions at the crosslinking points or nodes between SWCNTs. As a result, these SWCNT aerogels were mechanically fragile and underwent plastic deformation if compressed by more than 10%.[6] Likewise, foams of h-BN, fabricated using 3D porous structures as sacrificial templates, displayed high thermal conductivity and resistance to oxidation,[18,27,28] stemming from innate h-BN properties. However, most 3D h-BN foams are brittle with low mechanical strength.[15,16,18,29] Foams from h-BN and SWCNTs may possess the properties of SWCNTs and h-BN as well as emergent properties resulting from interactions between h-BN with SWCNTs and/or organization of h-BN around SWCNTs. Such composite foams are challenging to fabricate due to the binary composition and limited precursor availability of h-BN, and consumption of carbon from SWCNTs during h-BN synthesis that leads to damages to nanotubes.[18,30]

Herein, we report fabrication of elastomeric, freestanding, and mechanically robust aerogels of h-BN and SWCNTs via in-situ growth of h-BN on prefabricated SWCNT aerogels at relatively low temperature without degrading SWCNTs. We used a combination of high-resolution electron microscopy imaging, Raman spectroscopy

Department of Materials Science and Engineering, Carnegie Mellon University, 5000 Forbes Avenue, Pittsburgh, PA 15213, USA. E-mail: mohammad@cmu.edu
Electronic supplementary information (ESI) available: high-resolution TEM images, surface area and pore characteristics, electrical conductivity, and mechanical characteristics of h-BN/SWCNT aerogels.

and X-ray photoelectron spectroscopy (XPS) to characterize microstructure of the h-BN/SWCNT aerogels, chemical composition and bonding between h-BN and SWCNTs. Finally, we assessed the transformation of fragile SWCNT aerogels into elastomeric aerogels after h-BN coating by measuring the mechanical response of composite aerogels.

Results and discussion

The major steps in synthesis of h-BN/SWCNT aerogels are illustrated in Fig. 1. We began the fabrication of h-BN/SWCNT aerogels by infiltrating 100 mM aqueous solution of H_3BO_3 (99.99% metals basis Boric acid; Alfa-Aesar), a precursor for boron, into preformed, freestanding SWCNT networks in water, i.e., SWCNT hydrogels. A photograph of a SWCNT hydrogel of cylindrical shape is shown in Fig. 1. Images from high-resolution transmission electron microscopy (TEM) of cross-sections of SWCNT aerogels prepared from these hydrogels confirmed porous and isotropic SWCNT networks (Fig. 2a and 2b). The bundles in the images were likely an artifact of sample preparation for high-resolution TEM imaging which involved powdering of aerogels, dispersing in ethanol and then spraying onto a TEM grid. We then increased the temperature of H_3BO_3 filled SWCNT hydrogels to 100 ˚C and maintained at this temperature for 24 hours, which caused H_3BO_3 to dehydrate and form spherical B_2O_3 nanoparticles on SWCNTs,[30,31] which we refer to as B_2O_3/SWCNT hydrogels. High-resolution TEM imaging revealed that most of the B_2O_3 nanoparticles were located at the nodes and had diameters of 5-10 nm (Fig. S1a). Some of the B_2O_3 nanoparticles also formed on SWCNT struts and had much smaller diameters of ~1 nm (Fig. S1b). We point out that the SWCNTs were not chemically functionalized and B_2O_3 were not covalently linked to the SWCNTs. Next, we replaced water in the hydrogel with anhydrous ethanol and subsequently dried using a critical point dryer (Autosamdri 815, Tousimis) to obtain an aerogel of SWCNTs decorated with B_2O_3 nanoparticles. Finally, we converted the B_2O_3 nanoparticles into h-BN via pyrolysis at 1000 ˚C for 1 hr in N_2 atmosphere. The h-BN amount on the SWCNTs can readily be tuned by multiple coating of these h-BN/SWCNT aerogels with additional h-BN following the procedure outlined above. The typical density of h-BN/SWCNT aerogels used in this work was 13-15 mg/mL, which corresponds to a volume fraction of ~0.0092, with 7 mg/mL (volume fraction ~0.0054) of nanotubes and the rest h-BN, yielding a porosity of >99%. This h-BN coating procedure preserves the morphology of the initial network, allowing for fabrication of various shapes and sizes of h-BN/SWCNT aerogels (inset in Fig. 1).

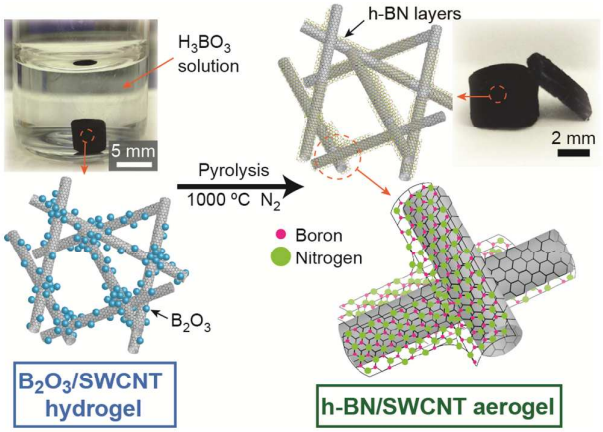

Fig. 1 Schematic illustration of synthesis procedure of h-BN/SWCNT aerogels.

We examined the microstructure of h-BN/SWCNT aerogels including the uniformity of h-BN coating, specific surface area (SSA), and the pore size distributions. Typically, transformation of B_2O_3 to h-BN is achieved at a pyrolysis temperature between 1300 to 1700 °C.[30,32] Surprisingly, the h-BN layers on SWCNTs were highly crystalline (Fig. 2) even though we used a relatively low pyrolysis temperature of 1000 °C. A comparison between high-resolution TEM images of cross-sections of SWCNT (Fig. 2a) and h-BN/SWCNT aerogels (Fig. 2c) showed that the h-BN coating did not alter the microstructure of the underlying SWCNT networks. Furthermore, images of isolated struts clearly showed SWCNTs at the center of the struts that were coated with multiple h-BN layers (cf. Fig. 2b with Fig. 2d and Fig. S1) organized parallel to the SWCNT surfaces. However, the h-BN coating was somewhat heterogeneous with nearly all of the nodes between the SWCNTs were covered with 2–10 h-BN layers and ~50% of the SWCNT struts were coated with 2–5 h-BN layers (Fig. 2d and S1). The more extensive coating of the nodes relative to the struts was likely because the B_2O_3 nanoparticles preferentially nucleated at the nodes, which have lower surface energy compared to the struts. The Brunauer-Emmett-Teller (BET) surface area measurement method[33] using nitrogen adsorption provided an SSA for h-BN/SWCNT aerogels of ~977 m^2/g, which is somewhat lower than the SSA of a SWCNT aerogel of ~1251 m^2/g due to h-BN coating the SWCNT surfaces and nodes (Figure S2a). The pore sizes and their distribution remained very similar to the same of SWCNT aerogels (Figure S2b). While TEM imaging is not suitable to discern actual pore structures within these aerogels because of the two dimensional representation of the depth of field in these microscopy techniques, we noticed from

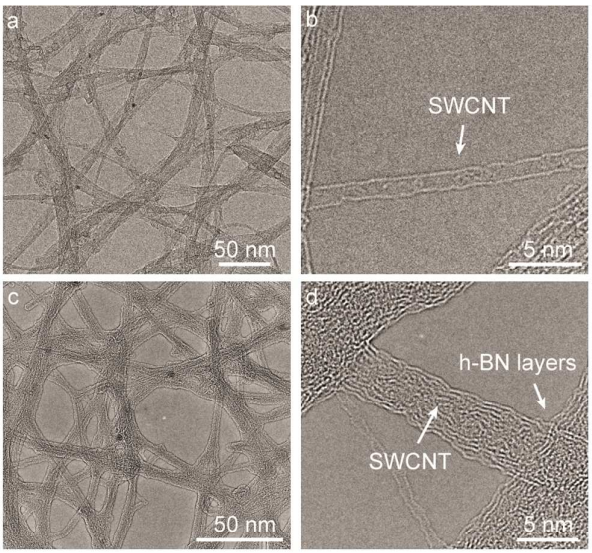

Fig. 2 High-resolution TEM images of cross-sections of pristine SWCNT and h-BN/SWCNT aerogels. (a, b) pristine SWCNT aerogels comprised of isotropic networks of mostly isolated and entangled SWCNTs. (c, d) h-BN coating did not alter the underlying SWCNT network microstructure, and the h-BN layers were organized parallel to the SWCNT surfaces, which were at the center of the struts.

high-resolution TEM images that a very small fraction of the pores became completely filled with h-BN (Fig. 2c and S1), which might have also reduce SSA.

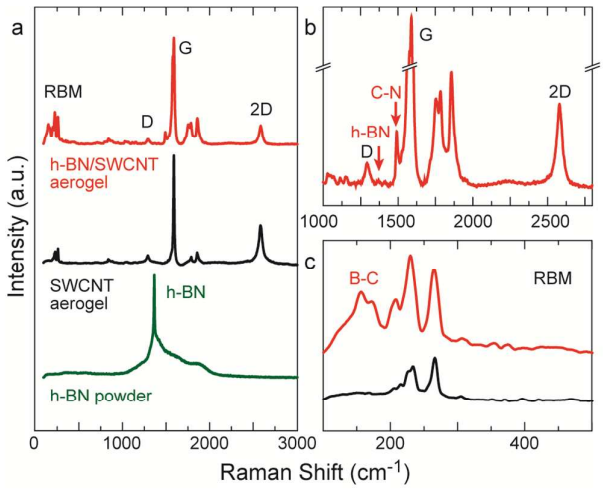

Fig. 3 Raman spectroscopy suggested that the h-BN coating did not damage SWCNTs. (a) Raman spectra of h-BN powder, pristine SWCNT aerogels and h-BN/SWCNT aerogels. The D, G and 2D bands in h-BN/SWCNT aerogels were characteristics of SWCNTs. The broadening of D and the G bands and the reduction in 2D band intensity in the Raman spectra from h-BN/SWCNT aerogels likely due to h-BN on SWCNTs. (b) Raman spectra from h-BN/SWCNT aerogels also displayed signatures associated with C-N bonds and h-BN structures. (c) RBM confirmed that SWCNTs remained undamaged by the h-BN coating. Furthermore, Raman spectra also showed signature of B-C bonds, which suggested formation of boron carbide during h-BN coating.

We further characterized the h-BN coating and validated the structural integrity of SWCNTs after the h-BN/SWCNT aerogel fabrication process using Raman spectroscopy (Fig. 3); note, intensity of each Raman spectrum was normalized to its G-band intensity, which represented the amount of sp^2-hybridized carbon within the aerogels. An increase in the intensity ratio between the G-band and the D-band, which characterized sp^3-hybridized carbon in the aerogels, would signify damages on SWCNTs. The intensity ratio of the G-band to the D-band was largely unchanged compared to pristine SWCNT aerogels, indicating little to no damage to SWCNTs during h-BN coating. Furthermore, Raman spectra displayed radial breathing modes (RBMs), which are attributed to SWCNTs, demonstrating that the SWCNTs remained intact in these h-BN/SWCNT aerogels. The Raman spectra from h-BN/SWCNT aerogels also showed unique Raman features associate with h-BN binding to SWCNTs. For example, both the D- and the G-band broadened after h-BN coating, possibly due to deposition of h-BN on SWCNTs.[34-36] Likewise, the intensity of the 2D-band, which represented the second-order two phonon process, was reduced, suggesting a stacking of a few layers of h-BN on SWCNTs.[37] However, the intensity of the Raman peak near at ~1366 cm^{-1}, which originated from the E_{2g} mode of B-N vibration and was clearly present in the h-BN powder (Fig. 3b), was very weak perhaps because h-BN/SWCNT aerogels contained very small amount of h-BN.[38] Finally, the Raman spectra also showed a peak at 1490 cm^{-1} (Fig. 3b), which we attribute to C-N bonds[39] that likely formed during the annealing of h-BN/SWCNT aerogels in N_2, and another peak near RBMs of SWCNTs (Fig. 3c), which denoted B-C bonds, suggesting presence of boron carbide within the h-BN/SWCNT aerogels.[40,41]

We next examined interactions between h-BN and SWCNTs by determining various bondings within h-BN/SWCNT aerogels using XPS (Fig. 4a-c). The 1s core level spectrum of carbon (C) can be deconvolved into three peaks with C-B peak at around 283.8 eV (curve 1 in Fig. 4a), C-C peak at 284.6 eV (curve 2 in Fig. 4a) and C-N peak at 285.3 eV (curve 3 in Fig. 4a).[42] The 1s core level spectrum of boron (B) can be deconvolved into the hexagonal B-N peak at 190.1 eV (curve 4 in Fig. 4b), which was the main bonding configuration for B,[43] and B-C peak at 188.7 eV (curve 1 in Fig. 4b). Note that if B-atoms are bound to oxygen atoms instead of N-atoms, the peak associated with this type of non-h-BN bonding are observed at higher binding energies.[44] The 1s core level spectrum of nitrogen (N) can be fitted into two peaks of which one of the peaks at 398.0 eV (curve 4 in Fig. 4c) can be attributed to hexagonal B-N,[45] and the other peak at 400.5 eV (curve 3 in Fig. 4c) can be attributed to C-N, which suggest that some of the N-atoms formed bonds with C-atoms. Overall, the 1s core level spectra of both B and N established that h-BN sheets are present within h-BN/SWCNT aerogels. Interestingly, the electrical conductivity of h-BN/SWCNT aerogels of ~0.78 S/cm was similar to that of pristine SWCNT aerogels of ~0.96 S/cm (Fig. S3), which suggested that the bondings between B and N

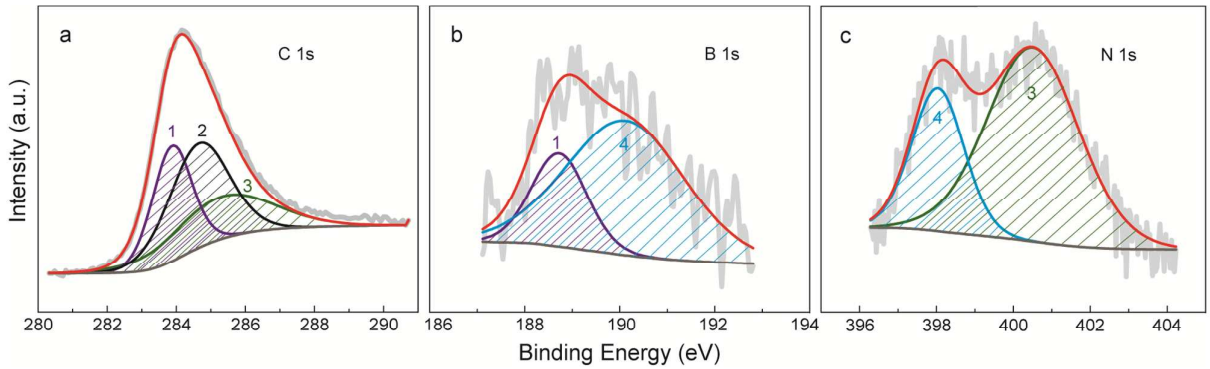

Fig. 4 X-ray photoelectron spectroscopy (XPS) spectra from h-BN/SWCNT aerogels showed bonding between h-BN and SWCNTs. 1s core levels of (a) carbon (C), (b) boron (B), and (c) nitrogen (N).

with SWCNTs were not extensive to disrupt continuous sp^2–hybridized carbon bonds in SWCNTs. Furthermore, the insulating h-BN probably did not infiltrate into the nodes and affected contacts between SWCNTs, which would drastically increase electrical resistance, but rather wrapped around the nodes (Fig. 2d and S1).

We assessed the effects of h-BN coating on the mechanical characteristics of SWCNT aerogels by measuring compressive stress (σ) as a function of compressive strain (ε) of h-BN/SWCNT aerogels at room temperature (~20 ˚C) (Fig. 5). Both pristine SWCNT aerogels of mass density ~7 mg/mL and h-BN/SWCNT aerogels of mass density of ~13 mg/mL could be compressed by more than 90% because of their high porosity. The σ versus ε curves showed three distinct deformation regimes, namely a Hookean or linear elastic regime for ε≤5%, a plateau regime for 5%<ε<40%, and a densification regime for ε≥40%; note, highly porous structures typically exhibit these mechanical deformation regimes under compression.[6,46] The SWCNT aerogels had a Young's modulus (*E*) of ~0.07 MPa, calculated from the Hookean regime, and underwent plastic deformation when compressed beyond ε=10%. We show σ versus ε curves for SWCNT aerogels up to ε=60% in Fig. 5a. We suspected that the SWCNTs were free to rotate around the existing nodes and created new nodes when compressed beyond the Hookean regime.[6] However, a lack of any restorative force that could destabilize the new nodes prevented original shape recovery. Please note that node formation within SWCNT networks costs little energy, but node removal requires overcoming a large van der Waals attraction.[47] In contrast, h-BN coating of SWCNT aerogels increased *E* by a factor of 2 to ~0.15 MPa, likely due to strengthening of the nodes and the struts through h-BN deposition. More strikingly, h-BN coating transformed the aerogels into elastomers – the h-BN/SWCNT aerogels completely recovered their original shaped when compressed up to ε=40%. The aerogels showed partial shape recovery for 40<ε≤60% with significant plastic deformation beyond this ε-range (Fig. 5a). For example, the aerogels showed ~30% plastic deformation during the first compression to 60%. Interestingly, the h-BN/SWCNT aerogels did not show any additional plastic deformation during any subsequent compression up to the 10th compression albeit with a reduced compressive strength (Fig. 5b and S4). We postulate that the h-BN coating of the nodes hindered free SWCNT rotations around the existing nodes, which resulted in an increase in *E*. At higher compressions, the h-BN at the nodes had to deform and when the load was removed, h-BN returned to their pre-compressed configurations, aiding the aerogels to spring back to the original shapes. The limited chemical bonding between h-BN and SWCNTs and van der Waals interactions likely prevented complete displacement of h-BN layers from the nodes. The plastic deformations during the first cycle observed for h-BN/SWCNT aerogels at compressions ε>40% were likely because of reorganization and/or permanent deformation of h-BN layers. Note that the negative loads observed during unloading for some of the σ versus ε curves might be due to high adhesive forces between the aerogels and compression heads.[48]

Experimental

Fabrication of pristine SWCNT hydrogels

The SWCNT hydrogels were fabricated using CoMoCAT (CG200; SouthWest NanoTechnologies, Inc.) SWCNTs that have diameters of 1.01 ± 0.3 nm and lengths of ~1 µm, as per manufacturer specifications. Methods for making various SWCNT networks have been reported elsewhere.[6,47,49,50] Briefly, SWCNTs were mixed with sodium dodecylbenzene sulfonate (SDBS; Acros Organics) in deionized water at a weight ratio of 1:10 to create SWCNT suspensions of concentration 1 mg/mL.[51] The SWCNT suspensions were sonicated using a probe sonicator (Thermo Fisher 500) for 2 hours at a power of 60 W and then ultracentrifuged at 125,000g (Beckman Coulter Optima™ L-100K) and at 10 °C for 19 minutes to separate any SWCNT bundles or impurities as sediment from the individually dispersed SWCNTs that remained in the supernatant. The SWCNT concentration in the

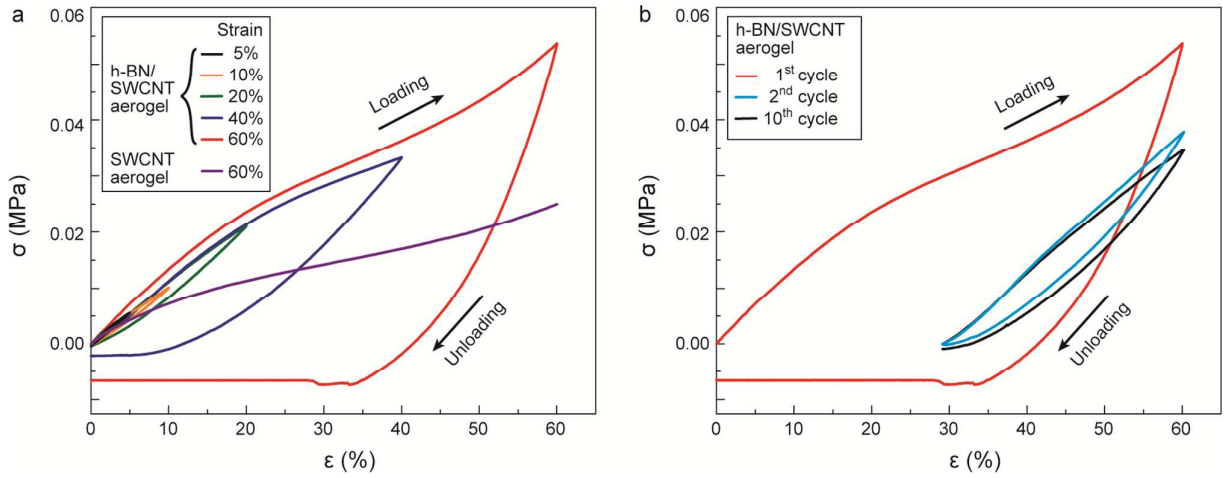

Fig. 5 Compressive stress (σ) versus strain (ε) curves for pristine SWCNT and h-BN/SWCNT aerogels during loading-unloading cycles. (a) Compressive loading of Pristine SWCNT aerogels and loading-unloading cycles for h-BN/SWCNT aerogels. (b) h-BN/SWCNT aerogels showed substantial plastic deformation during the first cycle when compressed by ε = 60% but did not show any additional permanent deformation during subsequent compressive loading-unloading cycles at least for 10 cycles for the same e with respect to initial sample dimensions.

supernatant was determined by measuring UV-vis-NIR absorbance using a spectrometer (Varian Cary 5000) and using an extinction coefficient of 2.6 (absorbance·mL)/mg·mm) at 930 nm.[6] We then evaporated water from the SWCNT dispersions at 60 °C until SWCNTs formed hydrogels at a concentration of 0.3 wt%. We liquefied the hydrogels and transferred into molds of cylindrical shape; the gels reformed within the molds in 12 hours. Residual surfactant was removed from the hydrogel by weak acid-treatment (1 M HNO_3) for 20 minutes. We then rinsed the hydrogels many times with water over the course of several hours and once with 1 M HNO_3 for 1 hour to remove the surfactant, followed by thorough washing with deionized water to remove HNO_3. Energy-dispersive X-ray spectroscopy measurements on similarly produced gels showed that our fabrication process removed all surfactants and metal impurities from nanotubes.[6]

Microstructure characterization

The microstructure of the both pristine SWCNT and h-BN/SWCNT aerogels were imaged using electron microscopy. We used a Tecnai F20 at 200 kV to collect low resolution TEM images and a FEI Titan 83 at 300 kV to collect HR-TEM images.

X-ray photoelectron spectroscopy (XPS) data were obtained with a DESA 150 analyzer (Staib instruments) and a TX400/2 X-ray gun (PSP vacuum technology) using an Al Kα X-rays. Elemental analysis was carried out using CasaXPS. Peak fitting was determined with a target of <1.2 eV FWHM for each peak.

The Raman spectra were collected using an inverted Raman confocal microscope (inVia Raman microscope, Renishaw) with a 50x objective of numerical aperture (N.A.) of 0.75 (Leica Microsystems) and a laser of wavelength 785 nm (1.58 eV). Laser power was set to 10 mW to avoid heat induced damage to the samples and the laser beams had a spot size of 1-2 mm. We collected 10 scans each at five different locations for each sample with an exposure time of 3 seconds and averaged the scans to improve signal to noise ratio. All data was collected and analyzed using WiRE software (Renishaw). Each Raman spectra was then normalized by its G-band intensity.

The SSA was calculated from nitrogen adsorption-desorption isotherms at 77 K, which were measured using a surface area measurement system (Gemini VII 2390 surface area analyser, Micromeritics), using the BET theory. The pore diameter ($2r$), pore volume (V), and pore diameter distribution (dV/dr) were calculated by applying the Barrett–Joyner–Halenda (BJH) method to the desorption branch of the isotherms.

The electrical conductivity of both SWCNT and h-BN/SWCNT aerogels were measured by attaching copper wire leads to the flat surfaces of rectangular aerogels with silver paste (DuPont 4929N) and then using a two-probe direct current measurements using EC-Lab V10 (BioLogic SP 200).

Measurements of mechanical properties

The compressive mechanical measurements were performed using an Instron 5943 equipped with a 50 N load cell. The aerogel samples used for compression measurements had cylindrical shape with a diameter of ~6 mm and a height of ~3 mm. The samples were loaded between two compression heads with the top head applying uniaxial compression at using a strain rate of 0.5 mm/min at room temperature. We applied a 5% prestrain to make a uniform flat contact between the compression heads and the samples and to prevent slipping of the samples.

Conclusions

We have fabricated and characterized freestanding, mechanically robust, and elastomeric composite aerogels of h-BN and SWCNTs. The composite aerogels had Young's modulus that were ~100% larger than that of SWCNT aerogels, and recovered their shapes after being compressed by more than 50%. Our fabrication methodology, which integrated solution based h-BN coating process with inherently flexible aerogel synthesis, maintained the ultracompressibility, high porosity, and morphology of the SWCNT aerogels but added elastomeric recovery to the composites. Our robust and facile fabrication scheme combined with appropriate ceramic-precursor will allow preparation of porous composites of various ceramic materials and SWCNTs including fragile SWCNT films.[52,53]

Acknowledgements

The authors thank T. Nuhfer for his assistance with TEM. This work was supported by the National Science Foundation through grant CMMI-1335417.

Notes and references

1 J. Banhart, *Progress in Materials Science*, 2001, 46, 559-632.
2 X. H. Cao, Y. M. Shi, W. H. Shi, G. Lu, X. Huang, Q. Y. Yan, Q. C. Zhang and H. Zhang, *Small*, 2011, 7, 3163-3168.
3 M. E. Davis, *Nature*, 2002, 417, 813-821.
4 L. L. Jiang and Z. J. Fan, *Nanoscale*, 2014, 6, 1922-1945.
5 K. H. Kim, Y. Oh and M. F. Islam, *Nature Nanotechnology*, 2012, 7, 562-566.
6 K. H. Kim, Y. Oh and M. F. Islam, *Advanced Functional Materials*, 2013, 23, 377-383.
7 M. A. Shannon, P. W. Bohn, M. Elimelech, J. G. Georgiadis, B. J. Marinas and A. M. Mayes, *Nature*, 2008, 452, 301-310.
8 D. W. Wang, F. Li, M. Liu, G. Q. Lu and H. M. Cheng, *Angewandte Chemie-International Edition*, 2008, 47, 373-376.
9 L. Zhang, F. Zhang, X. Yang, G. K. Long, Y. P. Wu, T. F. Zhang, K. Leng, Y. Huang, Y. F. Ma, A. Yu and Y. S. Chen, *Scientific Reports*, 2013, 3, 1408.
10 Y. Zhao, J. Liu, Y. Hu, H. H. Cheng, C. G. Hu, C. C. Jiang, L. Jiang, A. Y. Cao and L. T. Qu, *Advanced Materials*, 2013, 25, 591-595.
11 Y. W. Zhu, S. Murali, W. W. Cai, X. S. Li, J. W. Suk, J. R. Potts and R. S. Ruoff, *Advanced Materials*, 2010, 22, 3906-3924.

12 M. B. Bryning, D. E. Milkie, M. F. Islam, L. A. Hough, J. M. Kikkawa and A. G. Yodh, *Adv. Mater.*, 2007, 19, 661-664.
13 K. H. Kim, M. Vural and M. F. Islam, *Adv. Mater.*, 2011, 23, 2865-2869.
14 N. C. Hilyard and A. Cunningham, *Low density cellular plastics - Physical basis of behaviour*, Chapman and Hall, London, UK, 1994.
15 D. A. Lindquist, T. T. Borek, S. J. Kramer, C. K. Narula, G. Johnston, R. Schaeffer, D. M. Smith and R. T. Paine, *Journal of the American Ceramic Society*, 1990, 73, 757-760.
16 M. Rousseas, A. P. Goldstein, W. Mickelson, M. A. Worsley, L. Woo and A. Zettl, *Acs Nano*, 2013, 7, 8540-8546.
17 Z. Y. Wu, C. Li, H. W. Liang, J. F. Chen and S. H. Yu, *Angewandte Chemie-International Edition*, 2013, 52, 2925-2929.
18 J. Yin, X. M. Li, J. X. Zhou and W. L. Guo, *Nano Letters*, 2013, 13, 3232-3236.
19 K. H. Kim, Y. Oh and M. F. Islam, *Nature Nanotech.*, 2012, 7, 562-566.
20 K. H. Kim, Y. Oh and M. F. Islam, *Adv. Func. Mater.*, 2013, 23, 377-383.
21 D. N. Futaba, K. Hata, T. Yamada, T. Hiraoka, Y. Hayamizu, Y. Kakudate, O. Tanaike, H. Hatori, M. Yumura and S. Iijima, *Nature Materials*, 2006, 5, 987-994.
22 Z. Xu, Y. Zhang, P. G. Li and C. Gao, *Acs Nano*, 2012, 6, 7103-7113.
23 C. Y. Zhi, Y. Bando, C. C. Tang, H. Kuwahara and D. Golberg, *Advanced Materials*, 2009, 21, 2889-2893.
24 S. Vinod, C. S. Tiwary, P. A. D. Autreto, J. Taha-Tijerina, S. Ozden, A. C. Chipara, R. Vajtai, D. S. Galvao, T. N. Narayanan and P. M. Ajayan, *Nature Communications*, 2014, 5.
25 R. T. Paine and C. K. Narula, *Chemical Reviews*, 1990, 90, 73-91.
26 Y. Zhao, C. G. Hu, Y. Hu, H. H. Cheng, G. Q. Shi and L. T. Qu, *Angewandte Chemie-International Edition*, 2012, 51, 11371-11375.
27 Y. Chen, J. Zou, S. J. Campbell and G. Le Caer, *Applied Physics Letters*, 2004, 84, 2430-2432.
28 D. Golberg, Y. Bando, Y. Huang, T. Terao, M. Mitome, C. C. Tang and C. Y. Zhi, *Acs Nano*, 2010, 4, 2979-2993.
29 M. Loeblein, R. Y. Tay, S. H. Tsang, W. B. Ng and E. H. T. Teo, *Small*, 2014, 10, 2992-2999.
30 L. L. Chen, H. H. Ye and Y. Gogotsi, *Journal of the American Ceramic Society*, 2004, 87, 147-151.
31 S. Kocakusak, K. Akcay, T. Ayok, H. J. Koroglu, M. Koral, O. T. Savasci and R. Tolun, *Chemical Engineering and Processing*, 1996, 35, 311-317.
32 S. Yuan, B. Toury, C. Journet and A. Brioude, *Nanoscale*, 2014, 6, 7838-7841.
33 S. Brunauer, P. H. Emmett and E. Teller, *Journal of the American Chemical Society*, 1938, 60, 309-319.
34 K. McGuire, N. Gothard, P. L. Gai, M. S. Dresselhaus, G. Sumanasekera and A. M. Rao, *Carbon*, 2005, 43, 219-227.
35 Q. H. Yang, P. X. Hou, M. Unno, S. Yamauchi, R. Saito and T. Kyotani, *Nano Letters*, 2005, 5, 2465-2469.
36 X. X. Yang, L. Liu, M. H. Wu, W. L. Wang, X. D. Bai and E. G. Wang, *Journal of the American Chemical Society*, 2011, 133, 13216-13219.
37 Z. Liu, L. Song, S. Z. Zhao, J. Q. Huang, L. L. Ma, J. N. Zhang, J. Lou and P. M. Ajayan, *Nano Letters*, 2011, 11, 2032-2037.
38 R. V. Gorbachev, I. Riaz, R. R. Nair, R. Jalil, L. Britnell, B. D. Belle, E. W. Hill, K. S. Novoselov, K. Watanabe, T. Taniguchi, A. K. Geim and P. Blake, *Small*, 2011, 7, 465-468.
39 W. Q. Han, H. G. Yu and Z. X. Liu, *Applied Physics Letters*, 2011, 98, 203112.
40 S. Suzuki and H. Hibino, *Carbon*, 2011, 49, 2264-2272.
41 J. Q. Wei, B. Jiang, Y. H. Li, C. L. Xu, D. H. Wu and B. Q. Wei, *Journal of Materials Chemistry*, 2002, 12, 3121-3124.
42 L. Wang, P. Yu, L. Zhao, C. G. Tian, D. D. Zhao, W. Zhou, J. Yin, R. H. Wang and H. G. Fu, *Scientific Reports*, 2014, 4.
43 L. Ci, L. Song, C. H. Jin, D. Jariwala, D. X. Wu, Y. J. Li, A. Srivastava, Z. F. Wang, K. Storr, L. Balicas, F. Liu and P. M. Ajayan, *Nature Materials*, 2010, 9, 430-435.
44 X. J. J. Dai, Y. Chen, Z. Q. Chen, P. R. Lamb, L. H. Li, J. du Plessis, D. G. McCulloch and X. G. Wang, *Nanotechnology*, 2011, 22.
45 Y. Miyamoto, A. Rubio, M. L. Cohen and S. G. Louie, *Physical Review B*, 1994, 50, 4976-4979.
46 L. J. Gibson and M. Ashby, *Cellular Solids: Structure and Properties*, Cambridge University Press, Cambridge, U.K., Second edn., 1997.
47 L. A. Hough, M. F. Islam, P. A. Janmey and A. G. Yodh, *Physical Review Letters*, 2004, 93.
48 A. Skarmoutsou, C. A. Charitidis, A. K. Gnanappa, A. Tserepi and E. Gogolides, *Nanotechnology*, 2012, 23, 505711.
49 M. B. Bryning, D. E. Milkie, M. F. Islam, L. A. Hough, J. M. Kikkawa and A. G. Yodh, *Advanced Materials*, 2007, 19, 661-664.
50 K. H. Kim, M. Vural and M. F. Islam, *Advanced Materials*, 2011, 23, 2865-2869.
51 M. F. Islam, E. Rojas, D. M. Bergey, A. T. Johnson and A. G. Yodh, *Nano Letters*, 2003, 3, 269-273.
52 J. M. Harris, J. Y. Huh, M. R. Semler, T. Ihle, C. M. Stafford, S. D. Hudson, J. A. Fagan and E. K. Hobbie, *Soft Matter*, 2013, 9, 11568-11575.
53 M. R. Semler, J. M. Harris and E. K. Hobbie, *Journal of Chemical Physics*, 2014, 141.